ACS APPLIED ENERGY MATERIALS

www.acsaem.org Article

Operando Particle-Scale Characterization of Silicon Anode Degradation during Cycling by Ultrahigh-Resolution X-ray Microscopy and Computed Tomography

Paul Choi, Bharathy S. Parimalam, Laisuo Su, B. Reeja Jayan, and Shawn Litster*

Cite This: https://dx.doi.org/10.1021/acsaem.0c02823 Read Online

ACCESS | Metrics & More | Article Recommendations | Supporting Information

ABSTRACT: A combination of two-dimensional (2D) *operando* transmission X-ray radiograph sequences and three-dimensional (3D) *in situ* X-ray computed tomography was used to characterize a composite silicon anode during cycling in an electrode and coin cell format consistent with commercial lithium-ion (Li-ion) batteries. Silicon (Si) particle expansion and phase transformation within the porous electrode were imaged continuously during cycling at various rates at O(100 nm) resolution within a large O(100 μm) region of interest that capture electrode-scale effects. The imaging utilizes the substantial change in the 8 keV X-ray absorption coefficient with lithium (Li) alloying of Si during charging. At low rate cycling, the X-ray signal attenuation over the Si particles decreased with increased lithiation. In contrast, at high rate cycling, we observe increased attenuation at the electrode scale. A useful feature of this *operando* imaging is the simultaneous imaging of a large number of particles in close proximity. To capture the transformations of such a large number of Si during cycling, we introduce a standard deviation analysis of the *operando* transmission X-ray radiograph sequences. At key instances in the cycling, the same region of interest from the radiographs was reconstructed into 3D volumes. Si particle fracture, electrode expansion, and particle detachment from the current collector were all observed in the reconstructed volumes. This study demonstrates the unique capability of the combined 2D *operando* and 3D *in situ* X-ray imaging techniques in investigating the dynamic behavior of battery materials at the sub-micrometer particle scale in commercially relevant electrode formats.

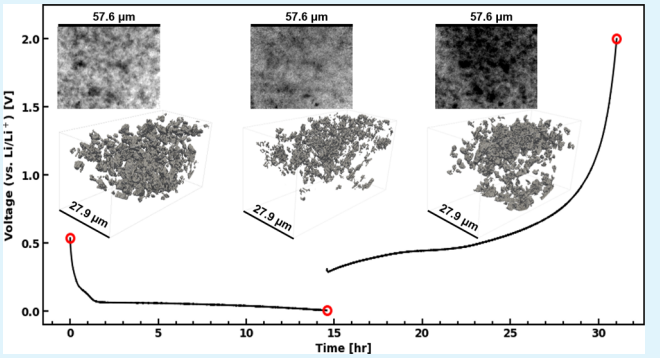

KEYWORDS: *lithium-ion battery, silicon anode, time-resolved, high-resolution, operando X-ray microscopy, in situ X-ray computed tomography*

INTRODUCTION

Since their initial commercial release by Sony and Asahi Kasei in the year 1991, lithium-ion batteries (LIBs) underwent widespread implementation owing mainly to their high energy density and good capacity retention. LIBs have enabled significant advancements in portable electronics technology and rapidly became the energy storage solution of choice for devices such as smartphones and laptop computers.[1] In the past decade, however, the increasing drive for electrification in the demanding transportation sector has revealed the need for a more advanced battery technology that will satisfy consumer demands for low cost, long range, and fast refueling time along with high reliability and durability.

Silicon (Si) is one of the most promising anode materials for replacing or enhancing the graphite used in almost every commercially deployed battery due to its exceptional specific capacity (3579 mA h g^{-1} at ambient temperature[2,3]), favorable discharge potential (ca. 0.4 V vs. Li/Li^+[4,5]), and natural abundance.[4] Successfully harnessing these advantages in a battery at high loading would greatly reduce its cost per specific energy and could accelerate a transformative shift from fossil fuels to renewable sources for the world's energy needs. However, the irreversible first-cycle capacity loss and poor cycle life caused by dramatic volumetric expansion (up to 310%[6,7]) and the eventual fracturing/pulverization of Si upon alloying with lithium (Li) hinder practical implementation of anodes with high Si loading.[8−10]

This establishes a need for targeted approaches to mitigating the negative side effects of Li−Si alloy phase cycling, which requires an enhanced understanding of its mechanism. Toward this goal, prior studies have characterized the structural changes of Si-incorporated electrodes during operation by

Received: November 12, 2020
Accepted: January 26, 2021

https://dx.doi.org/10.1021/acsaem.0c02823
ACS Appl. Energy Mater. XXXX, XXX, XXX−XXX

electron microscopy,[8,11,12] atomic force microscopy (AFM),[6,13,14] and microscale X-ray computed tomography (micro-CT).[15−19] These characterization techniques, however, present notable limitations: electron microscopy requires a vacuum environment that limits the use of liquid or gel electrolytes in the sample, AFM characterization is limited to the surface that its probe can access, and micro-CT may be limited by its spatial resolution (ca. 1−2 μm). In addition, the electron microscopy and AFM methods require electrodes, electrolytes, or cell arrangements that are substantially different from those present in commercial batteries. Recently, nano-scale X-ray computed tomography (nano-CT) was used to characterize the cycling-induced morphological evolution of a Si-based electrode: high-resolution reconstructions of the electrode at various stages of cycling were used to identify changes in its morphological characteristics (e.g., specific surface area).[20] A limitation of this *in situ* imaging is that it misses the transient mechanisms leading to intermittently imaged states, and some effects and transient states with fast relaxation times can be missed.

In this work, two modes of nano-resolution X-ray characterization are employed to investigate Li−Si phase cycling: (1) *in situ* three-dimensional (3D) volumetric reconstruction via computed tomography and (2) *operando* two-dimensional (2D) transmission X-ray microscopy (TXM) in temporal sequence. As a result, a comprehensive characterization of the Si electrode before, during, and after cycling is presented for the first time.

EXPERIMENTAL SECTION

The Li−Si half-cell used for this study was assembled inside an argon-filled glovebox whose oxygen and water levels were maintained below 0.5 ppm. The schematic and the prepared cell are shown in Figure 1. Standard CR1220-type coin cell casings were modified with 8 mm-wide, 1.5 mm-tall rectangular slots to allow for minimally obstructed X-ray transmission and tomography scans. Kapton sheets were attached to the inside of the cutouts using an EA E-60HP (Loctite, Düsseldorf, Germany) adhesive to seal the battery components from atmospheric exposure. The Si electrode was fabricated by blade-coating a mixture of 50:25:25 wt % Si microparticles (MTI Corporation, Richmond, CA, USA), polyacrylic acid binder (Sigma-Aldrich, St. Louis, MO, USA), and SUPER C65 carbon black (Imerys Graphite & Carbon, Bironico, Switzerland), respectively, on a 9 μm-thick copper foil. A 9 mm-diameter disk was punched out from the coated electrode, which resulted in the Si anode with an area and Si loading of 2.54 cm^2 and 0.835 mg, respectively. Li foil (MTI Corporation, Richmond, CA, USA) was hole-punched into 9 mm-diameter disks for use as the counter electrode. Celgard 2400 separators (Celgard LLC, Charlotte, NC, USA) were punched into 11 mm-diameter disks to prevent possible shorts that may occur during cell assembly due to electrode misalignment. A total of 100−150 μL of battery-grade 1.0 M $LiPF_6$ in EC/DMC (v/v = 1:1, Sigma-Aldrich, St. Louis, MO, USA) electrolyte was added prior to crimping the coin cell inside the glovebox. Fully assembled test cells rested for 24 h inside the glovebox to ensure thorough electrolyte distribution. The coin cell was mounted in a custom 3D-printed coin cell holder for CT imaging that allows rotation with the electrical wiring.

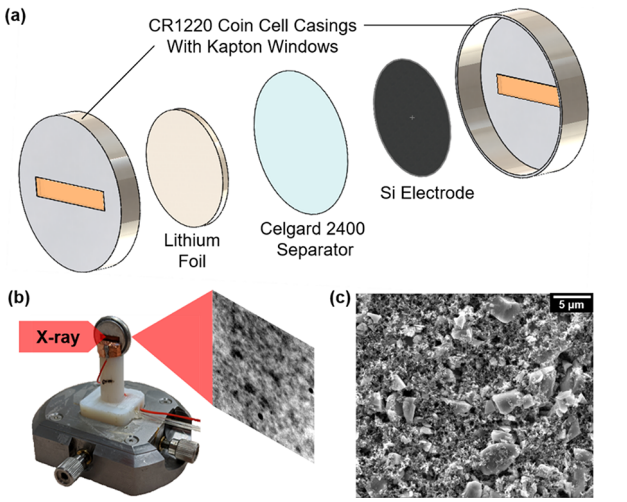

Figure 1. Custom coin cell setup for *operando* X-ray CT characterization. Exploded view of the *operando* coin cell (a) and the cell mounted on a 3D-printed cell holder for imaging in the nano-CT instrument (b). SEM image of the Si composite electrode in its pristine state (c).

The X-ray microscope (nano-CT) utilized for *operando* and *in situ* X-ray imaging was the UltraXRM-L200 (Xradia Inc., Pleasanton, CA, USA). The nano-CT generates X-rays with a photon energy of 8 keV using a rotating copper anode source, which pass through the slotted portion of the modified coin cell; the X-rays then reach the detector, which consists of a scintillator and a charge-coupled device (CCD) array, where they produce monochromatic radiographs. The *operando* 2D radiograph sequence was obtained with 30 s of exposure per image, 2-by-2 CCD pixel binning, and 0° X-ray angle of incidence with respect to the sample. The *in situ* 3D tomograms between *operando* cell cycling were obtained with 80 s of exposure per projection, 2-by-2 CCD pixel binning, and 325 projections between −65° and 65° X-ray angles of incidence. The radiographs and tomography scans were acquired using the instrument's large field of view and absorption contrast optics, which have a physical field of view of 65 μm by 65 μm and an optical resolution of 150 nm, similar to a pixel resolution of 130 nm with 2 × 2 binning. All radiographs were normalized using an average of 100 radiographs taken of air (background) prior to any post-processing. Preliminary experiments have demonstrated that there is no significant loss in capacity or beam damage due to exposing the cell to the X-ray beam.

The electrical load was applied and recorded with a potentiostat (SP-50, BioLogic, Seyssinet-Pariset, France) concurrently with the 2D *operando* radiograph sequences. The sample cell was tested with the following protocol in the listed order: (1) initial Si lithiation of Si at a current density of 0.063 mA cm^{-2} (~C/75 rate), (2) initial Si delithiation at a current density of 0.050 mA cm^{-2} (~C/93.5), (3) a second cycle at a current density of 0.157 mA cm^{-2} (~C/30), and (4) 13 cycles at a current density of 0.471 mA cm^{-2} (~C/10), with the capacity based on weighing and the theoretical capacity of Si. The applied current was determined and adjusted according to the desired temporal resolution of the *operando* cycling datasets. All cycles were conducted between 0.005 and 2 V with a 5 min open circuit following each lithiation/delithiation step. The sample cell remained mounted within the nano-CT instrument throughout the entirety of the experiment, where the ambient temperature is maintained to a range of 23−25 °C. The capacity of the electrode was determined by cycling a half cell with an electrode from the same coating in an identical cell configuration but fabricated with casings without the window modifications.

To accurately represent the changes observed during the *operando* tests, the 2D radiograph sequences were registered and cropped to a common region of interest without any of the gold fiducial microparticles that are placed on the electrode for metrology corrections during the reconstruction of the 3D CT images. As a result, the resulting radiograph sequences have a dimension of 454 pixels by 363 pixels (57.6 μm by 46.1 μm)—a 37% reduction. The corrected radiographs were then denoised and contrast-adjusted using a 3-by-3 median filter and signal thresholding, respectively. All post-processing of the 2D radiograph sequences was done using FIJI.[21] In particular, the registration was done using the "Template_Matching" plugin installed in FIJI.[22]

https://dx.doi.org/10.1021/acsaem.0c02823
ACS Appl. Energy Mater. XXXX, XXX, XXX−XXX

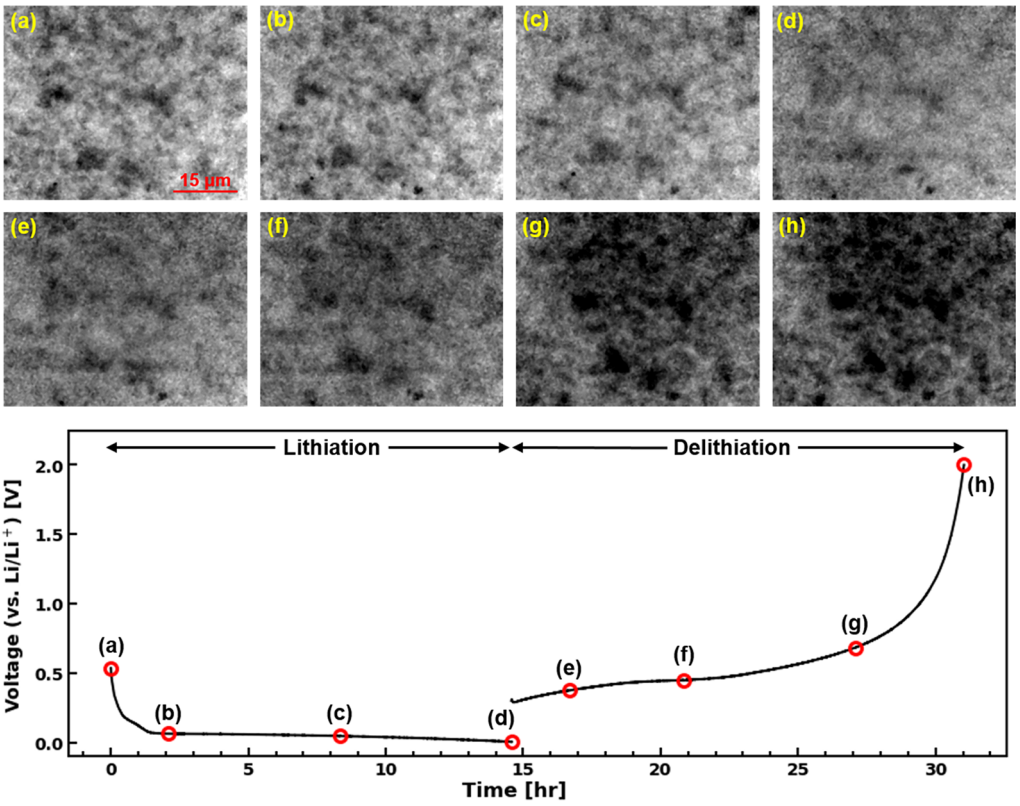

Figure 2. *Operando* TXM radiograph sequence of a Si half-cell during the first cycle and the corresponding cycling curve. The initial lithiation (a–d) and delithiation (e–h) were conducted at current densities of 0.063 and 0.050 mA cm^{-2}, respectively. All radiographs are images of the same region of interest of the Si electrode and therefore share the 15 μm scalebar shown in (a).

For 3D analysis, tomograms were computationally reconstructed into 3D volumes using TomoPy and ASTRA Toolbox.[23,24] Similar to the 2D datasets, the tomograms were first registered and cropped to a common region of interest. The corrected tomograms were then reconstructed into 3D volumetric structures using the GPU-based simultaneous iterative reconstruction technique. The resulting 3D reconstructions were denoised using a nonlocal means denoising technique[25] and then segmented using the 3D iterative thresholding technique via a FIJI plugin.[26] Last, the segmented volumetric structures of the Si electrode were visualized using Tomviz[27] and Dragonfly software (Object Research Systems, Montreal, Quebec, Canada).

RESULTS AND DISCUSSION

Initial Cycling of the Si Electrode in *Operando*. We first analyze the imaging from the initial low current density lithiation/delithiation cycle as it provides a quasi-equilibrium visualization of the Si particle structure evolution. Figure 2 shows the voltage of the cell as a function of time during this initial cycle; the Si lithiation was done at a current density of 0.063 mA cm^{-2} (~C/75 rate), and the subsequent Si delithiation was done at a current density of 0.050 mA cm^{-2} (~C/93.5). During the initial lithiation, the cell potential began its plateau near the 1.5 h mark (35.9 mA h g^{-1}) at approximately 0.070 V and decayed over the following 13 h. During the initial delithiation that followed after the 5 min open-circuit rest period, the cell potential plateaued between 0.3 and 0.5 V. The specific capacities of the initial lithiation and delithiation were 349.1 and 315.6 mA h g^{-1}, respectively. Although this capacity is ~20% of the theoretical specific capacity based on weighing (1790 mA h g^{-1} based on an approximate Si loading of 0.835 mg), a sufficient amount of that maximum capacity is accessed to assess the *operando* electrode and particle behavior. Using the same electrode sheets in a non-windowed cell, we obtained initial capacities >75% of the theoretical. Based on these comparisons of Kapton windowed vs non-windowed cells and recent improvements in cycling other battery chemistries with a nitrogen gas curtain flowing past the window *operando* cell, we attribute the low capacity to water and oxygen diffusion across the Kapton windows. The uneven pressure distribution in the cell due to the window modifications may also affect cell performance; however, characterizing the pressure effects on Si electrodes is beyond the scope of this investigation. A solution for future studies will be the use of thin metal foil instead of Kapton. Nevertheless, the capacity was sufficient to observe notable particle lithiation and delithiation as well as demonstrate the analysis approaches developed herein. Furthermore, despite the lower capacity, the battery performance is substantially more similar to a conventional cell in terms of materials and performance relative to many of the other ultrahigh-resolution *operando* imaging.[6,8,11,12,14]

During the initial cycle, a total of 3726 radiographs were collected, of which eight are shown in Figure 2a–h along with their corresponding points in the voltage time series. Video SV1 shows the transient process, and the interested reader is highly encouraged to view the online video as the transient evolution is more discernable in the video format. The contrast in the presented radiographs arises from the variation of X-ray absorption within the field of view. The degree of X-ray absorption can be characterized by the Beer–Lambert law, which strongly correlates the attenuation coefficient of an object to its density and atomic number: the denser and higher

https://dx.doi.org/10.1021/acsaem.0c02823
ACS Appl. Energy Mater. XXXX, XXX, XXX–XXX

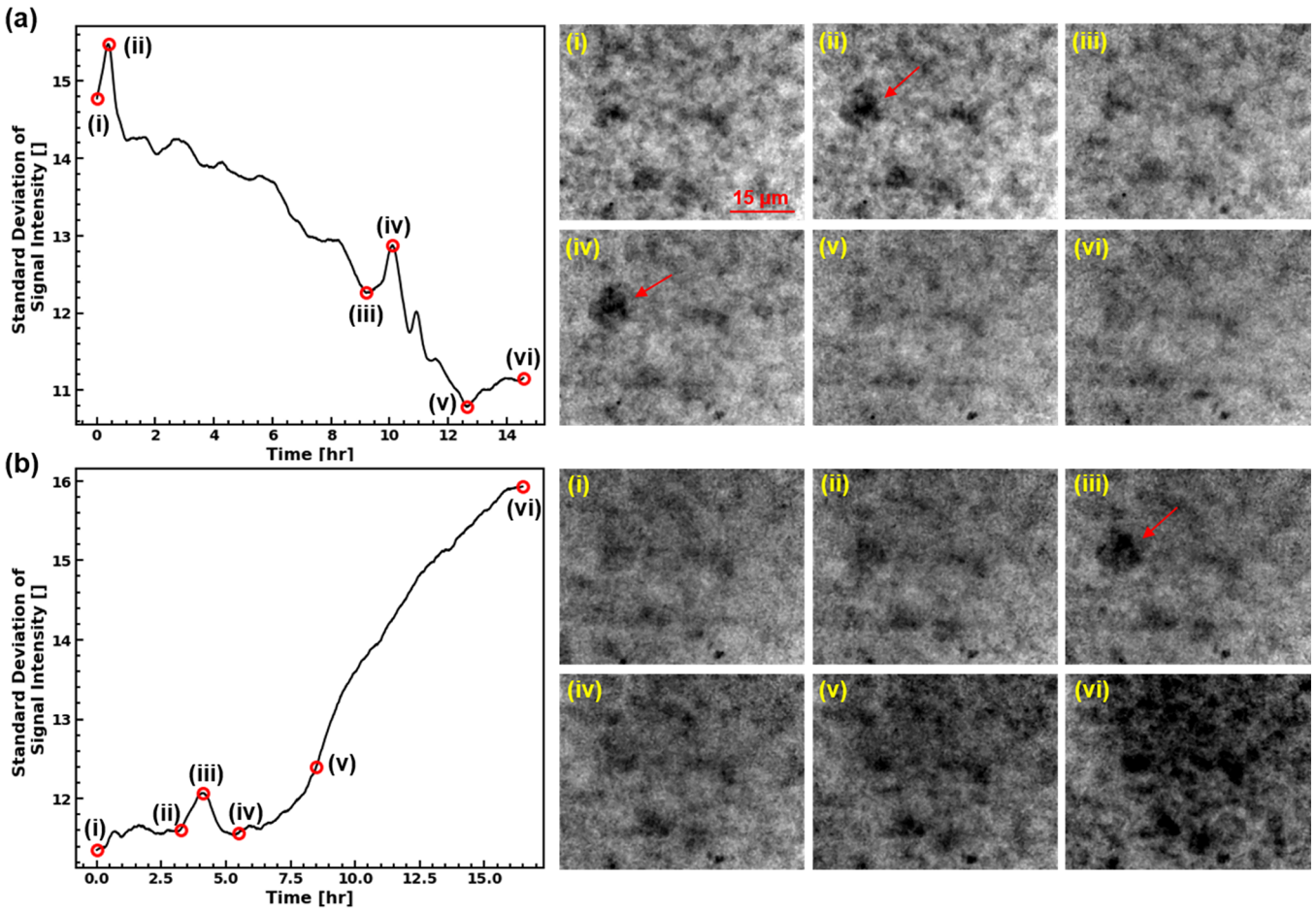

Figure 3. Standard deviation of the X-ray signal intensities from the *operando* TXM radiographs during the initial lithiation (a) and delithiation (b) is presented as time series alongside select frames corresponding to points of interest (i–vi). Peaks in the X-ray intensities observed at (a)(ii), (a)(iv), and (b)(iii) all appear to be caused by the erratic change in X-ray absorption of a single Si agglomerate.

atomic number the material, the more X-ray intensity will decrease. At 8 keV, the X-ray attenuation length (i.e., the characteristic depth into the material where the X-ray intensity has decreased, due to absorption, to about 37% (1/e) of the unattenuated intensity) through Si is approximately 66.4 μm. In contrast, the attenuation lengths of Li–Si alloys $Li_{2.5}Si$ and $Li_{3.75}Si$ are approximately 490 and 582 μm, respectively. The observer should keep in mind that the imaged changes in attenuation in radiographs are not as dramatic as those differences in attenuation lengths due to the corresponding increased volume and through-plane thickness with lithiation of Si, although there is some reduced absorption due to the in-plane expansion of the Si atoms.

Figure 2a is the through-plane radiograph of the tested Si electrode in its pristine state. The darker regions indicate a higher volumetric X-ray absorption, which can be attributed to a higher concentration of Si particles or large Si particles in that area. In contrast, the brighter regions are likely populated with a higher concentration of low atomic number components of the electrode (e.g., an electrolyte, conductive carbon, and PAA binder) that have much longer attenuation lengths. The distribution of the signal intensities in the field of view indicates an even distribution of the high-attenuation components (i.e., Si particles), with the exception of a few larger Si agglomerates. As Si lithiates, the Si particles undergo a series of phase transformations as they alloy with Li. It is reported that Si volumetrically expands up to 310% during this transformation[6,7] and ultimately forms $Li_{15}Si_4$ at room temperature.[2,3] Figure 2b–d captures the Si electrode during lithiation and reveals two observable changes: (1) homogenization of the signal intensities and (2) decreased signal overall. The first observed phenomenon can be attributed to the phase change itself: the alloyed phase of Si is less X-ray absorbing and the volumetric expansion causes the amount of Si atoms in the X-ray beam path to decrease significantly. The lack of particle-by-particle contrast apparent in Figure 2d, which is present in Figure 2a, is a manifestation of the said physical transformations. The second observed change in the average attenuation increasing with lithiation was not predicted. One possible explanation for this is the formation of the additional solid electrolyte interphase (SEI) with the greater surface area of the Li–Si alloy particles and the resulting deposition of X-ray absorbing elements (e.g., fluorine)[28] within the depth of focus. During delithiation, the physical changes observed in the radiographs are reversed. In Figure 2e–h, the mostly uniform field of view becomes repopulated with more X-ray absorbing features as the electrode shrinks, and Si returns to its original phase. The Si particles appear darker in Figure 2h than in Figure 2a, which possibly indicates a progression in the deposition of SEI byproducts as well as a possible preferential deposition in regions with a higher active material population.

https://dx.doi.org/10.1021/acsaem.0c02823
ACS Appl. Energy Mater. XXXX, XXX, XXX–XXX

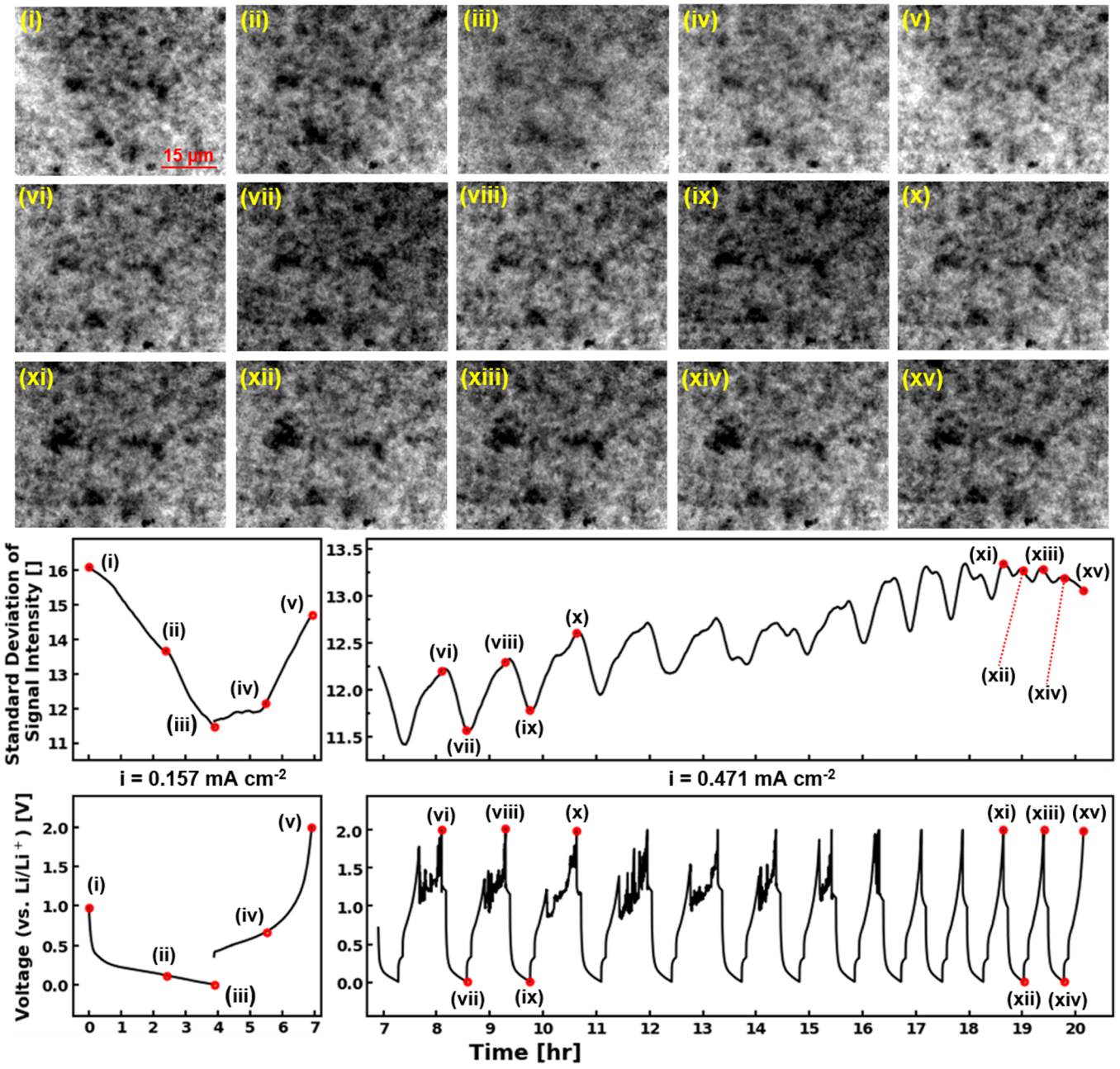

Figure 4. *Operando* TXM radiograph sequence and the time series of the X-ray signal standard deviation and cell voltage during higher current density cycling. The cell was cycled once at 0.157 mA cm^{-2} (i−v) and was subsequently cycled 13 times at 0.471 mA cm^{-2} (vi−xv). The non-uniform delithiation curve is likely caused by the exacerbation of the uneven electrode−separator interfacial pressure distribution caused by the lithiation-induced electrode expansion.

Standard Deviation Analysis of *Operando* Radiographs for Tracking Changes in Morphology. As demonstrated in Figure 2, the changes in the electrode morphology can be observed concurrently with the electrochemical response of the cell. However, the charging curves do not contain any information with which to identify and track major physical changes that are apparent in the radiographs. Ideally, we would be able to identify the changes in each particle's dimension and attenuation. However, with an electrode thickness consistent with commercial cells that results in many particles across the through-plane direction and in-plane overlap with expansion, a particle-by-particle analysis of the radiographs is not feasible. We explored characterization of image intensity histograms to quantify changes in the electrode. Although the histograms indicated the changes, it was more useful to show parameters of the histogram, such as mean and standard deviation. The standard deviation was found to give the clearest indications of changes in the electrode with charging and discharging, whereas the mean was less indicative due to long time-scale changes due to other factors. As shown in Figure 3, we demonstrate that the standard deviation of the radiographs' signal intensity can be used to track the stages of morphological changes in the Si electrode during cycling. The radiographs shown in Figure 3 are shown in Figure 2 but are, instead, presented alongside the signal standard deviation as a function of time. Figure 3a,b shows that the standard deviation of the radiograph signal is inversely correlated with the degree of electrode lithiation. As

https://dx.doi.org/10.1021/acsaem.0c02823
ACS Appl. Energy Mater. XXXX, XXX, XXX−XXX

the Si particles expand and become less X-ray absorbing at any point due to lithiation expansion, the contrast between Si and the surrounding less attenuating phases becomes less discernable. This means that the pixels within the radiograph have more similar intensity values, leading to a narrower distribution of intensities. The reverse of this explanation is also valid, as demonstrated in Figure 3b.

The standard deviation analysis can also reveal any sudden changes in morphology through sudden peaks. Figure 3a(i)–a(ii), a(iii)–a(iv), and b(ii)–b(iii) shows sudden peaks that deviate from the trend of the standard deviation curve. The corresponding radiographs reveal that these peaks occur when a large feature (many pixels) of either very high or low signal intensity appears or disappears within the field of view. In this particular case, all peaks can be attributed to the erratic change in volume of a large Si agglomerate, as pointed out in the radiographs of Figure 3a(ii), a(iv), and b(iii).

Furthermore, mapping the standard deviation of signal intensity during longer cycling at higher rates revealed the physical changes that can contribute to capacity decay. Video SV2 shows the *operando* TXM sequence of the higher rate cycling, whose select frames are analyzed and shown in Figure 4.

In Figure 4, the standard deviation of signal intensity is shown alongside the voltage curve and radiographs at select points. Points (i–x) in Figure 4 are consistent with the observations made in regard to Figure 3: the signal standard deviation decreases with lithiation and increases with delithiation. Points (xi–xv) correspond to the last two cycles at a current density of 0.471 mA cm^{-2} (~C/10), during which the capacity of the cell has decreased to approximately 52.7 mA h g^{-1} (vs 70.1 mA h g^{-1} of points (vi–x). The standard deviation of points (xi–xv) shows a complete deviation from the correspondence between the cycling curve and the standard deviation curve (e.g., peaks match with peaks) and a greatly reduced fluctuation. The lack of fluctuation in the standard deviation of the radiograph signal indicates that cycling the cell no longer induces the morphological changes observed in previous cycles. Radiograph frames (xi–xv) shows that the majority of the low-intensity Si particles remain unchanged both in shape and intensity in the last two cycles. As fewer Si particles lithiate and delithiate, as observed from the radiographs, fewer Si particles can contribute to the cycling capacity of the cell.

We propose that the standard deviation of these radiographs and their variation in time can be used as a metric for interrogating the local degradation of electrode materials during cycling studies by nano-CT. Figure 5 is a plot of the change in the image standard deviation between the start and end of each delithiation versus the delithiation capacity. As Figure 5 shows, the delithiation capacity of the electrode shows a clear correlation of capacity loss with a lower change in the standard deviation. In future studies, this method can be used to identify local regions of increased electrode degradation.

3D Volumetric Reconstructions of the Si Electrode Between Cycles. The 2D radiographs described above allow us to observe electrodes at a high temporal rate; however, as discussed above, the changes in individual particles are difficult to distinguish due to the through-plane overlap of particles in thick, commercially relevant electrodes. For this reason, we performed more time-intensive tomography scans at key points during cycling. Video SV3 shows the reconstructed raw 3D CT image of the electrode at six different states: pristine, after the

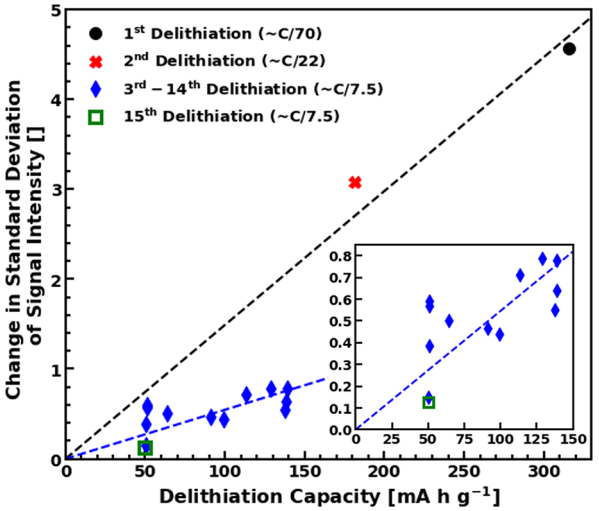

Figure 5. Change in the image standard deviation during every delithiation observed in *operando*. As delithiation capacity decreases, the change in the standard deviation is lowered. This trend indicates that fewer particles are converted back to the Si phase (higher attenuation) during delithiation as the delithiation capacity decays. The change in standard deviation decreases dramatically after the second cycle when the cycling rate was increased by approximately 193%, suggesting a correlation between the cycling rate and the rate of decay in the standard deviation change.

initial lithiation, after the initial delithiation, after the second lithiation, after the second delithiation, and at the end of the experiment. Figure 6 shows the orthogonal virtual slices of the reconstructed electrode in the pristine state before and after the first lithiation and after the first delithiation. As can be seen, the Si particles show a strong contrast in the pristine state, whereas the expansion and reduced attenuation of the particles after lithiation yields a much less clear boundary between particles. The deposition of electrolyte decomposition products and addition SEI with lithiation may also contribute to the loss of particle contrast. However, the volumetric contrast returns after delithiation as expected from the radiographs.

Figure 7 shows the segmented 3D volume reconstructions of the Si electrode at six different states within the same region of interest as the radiographs: (a) pristine, (b) after the initial lithiation, (c) after the initial delithiation, (d) after the second lithiation, (e) after the second delithiation, and (f) at the end of the experiment. In these images, the segmentations were done with thresholding at the intensity level that segmented discernable particles in each state. These 3D structures provide additional insights into the morphological changes observed in the 2D *operando* sequences. Figure 7a shows the pristine electrode that is densely packed with Si particles. The top surface of the reconstructed volume shown is approximately the interface with the separator, and the bottom surface extends to the current collector. After the initial lithiation, two significant observations can be made: (1) the distance between the electrode–separator interface and the field-of-view boundary has increased by 13% and (2) the reconstructed features are smaller, noisier, and preferentially distributed near the electrode–separator interface. The first observation is likely caused by the expansion of the electrode due to the lithiation of Si particles. The second observation can be attributed to partially lithiated Si particles whose cores still absorb enough X-ray signals to be resolved in the

https://dx.doi.org/10.1021/acsaem.0c02823
ACS Appl. Energy Mater. XXXX, XXX, XXX–XXX

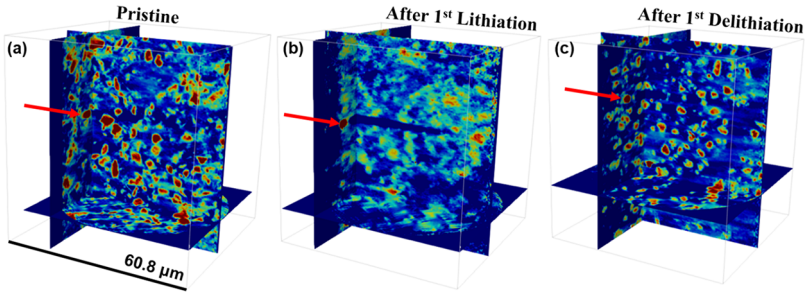

Figure 6. Orthogonal virtual slices of the reconstructed electrode in pristine (a), post 1st lithiation (b), and post 1st delithiation (c) states. The X-ray intensities of all three states were normalized to enable side-to-side visual comparison. The heatmap represents the degree of X-ray attenuation: colors red, green, and blue correspond to high, medium, and low attenuations, respectively. Si in the unlithiated state is clearly visible in deep red in both (a) and (c), whereas most discernable particles in (b) are of medium-low attenuations. A gold fiducial marker (pointed out with red arrows) placed on the electrode−separator interface was used to locate a region of interest for comparison. The scale bar shown in (a) is applicable to all states (a)−(c).

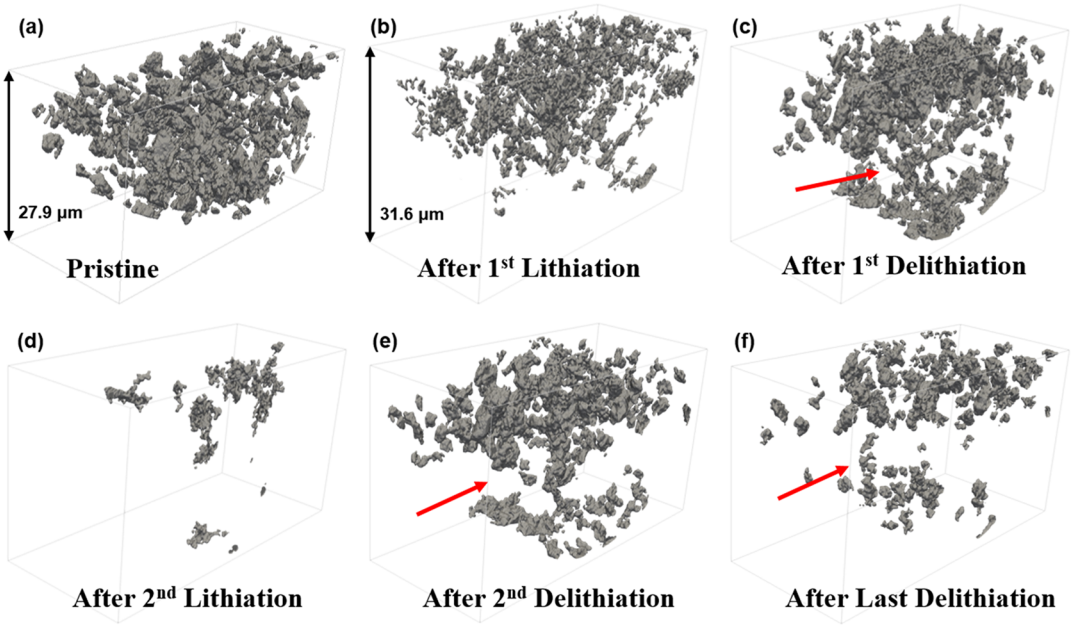

Figure 7. Computationally reconstructed and segmented 3D volume of the Si electrode at various states of operation. The height of the reconstructed volume, as shown in (a) and (b), represents the distance between the electrode−separator interface and the field-of-view boundary; this distance increases after the initial lithiation and remains throughout all cycles (b−f). This indicates a 13% irreversible height expansion of the electrode, which can also explain the voids observed in (c), (e), and (f).

reconstruction as distinct particles. The preferential distribution of the reconstructed particles after the initial lithiation may also indicate low electrical conductivity due to the uneven distribution of electrolyte or pressure inside the cell. Figure 7c shows the electrode after the subsequent delithiation. The reconstructed particles in this state are smaller and more spread out, with a noticeable void near the center of the volume. The void can also be a sign of the electrode expansion that may have occurred during the initial lithiation.

Figure 7d,e, respectively, shows the reconstructions at states after the second lithiation and delithiation. The fully lithiated phase of Si at room temperature ($Li_{15}Si_4$) is effectively transparent relative to pure Si due to the long attenuation length. It is thus possible that Figure 7d is indicative of the complete lithiation of most Si particles within the field of view except for some Si-rich cores. Figure 7e shows that after the second delithiation, the electrode is similar in structure to that of Figure 7c but contains fewer and smaller discernable particles. This does not mean that Si is no longer present, only that it is likely still in a lithiated state without sufficient contrast for segmentation. Smaller particles can be attributed to Si particle pulverization due to excessive volumetric change, and fewer reconstructed particles indicate possible loss of contact between lithiated particles and the current collector. Figure 7f shows the delithiated electrode after high rate cycling. In this case, the observations made about Figure 7e are exacerbated: the discernable reconstructed particles are even smaller and fewer in number. This is indicative of fewer Si particles undergoing the phase change as intended, which is consistent with the explanation for the decaying change in signal standard deviation on the last two cycles and the loss in capacity. In other words, the reduction in discernable particles that can be segmented by their contrast when the electrode is delithiated is indicative of the loss of active particles and capacity. For comparison, Figure 8 shows a plot of the total particle volume for pristine and delithiated segmented images versus the delithiation capacity of the cell. As can be seen, the loss in segmentable particle volume is consistent with the capacity

https://dx.doi.org/10.1021/acsaem.0c02823
ACS Appl. Energy Mater. XXXX, XXX, XXX−XXX

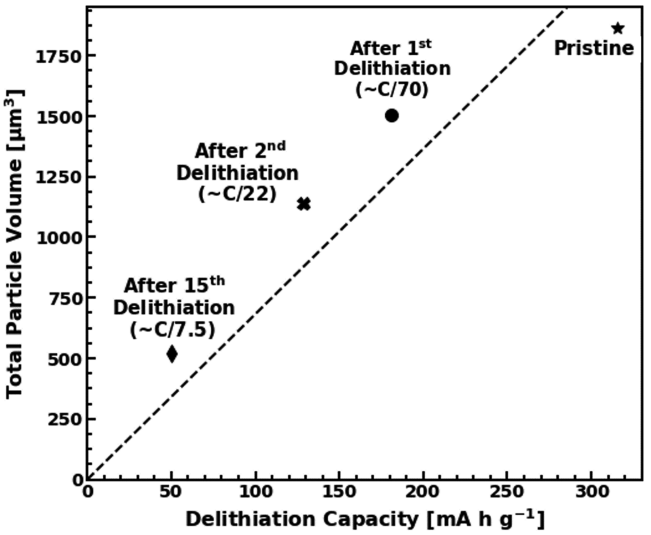

Figure 8. Total particle volumes from the segmented reconstructions are shown along with their respective delithiation capacities. The trend reveals that the loss in delithiation capacity is accompanied by a loss in segmentable particles in the volumetric reconstruction of the electrode. The loss in segmentable particles indicates that only a portion of the previously lithiated Si particles delithiate fully to the highly attenuating Si phase.

change. Thus, in addition to the radiography standard deviation change, the segmentable volume change with cycling can be used to interrogate regions of capacity loss in Si-based anodes.

CONCLUSIONS

We used a combination of 2D *operando* X-ray microscopy and 3D *in situ* X-ray computed tomography to study the dynamic morphological changes associated with Li−Si alloy phase cycling. The volumetric expansion and the formation of less X-ray absorbing phase of the Li−Si alloy were observed during lithiation under various current densities as well as the reverse phenomena during delithiation. We also showed the correlation between the standard deviation of the radiograph signal intensities and the degree of lithiation and used it to identify the evolution of Si particles during cycling. Furthermore, the decreasing peak-to-peak distance of the signal standard deviation in the *operando* radiographs was identified to be the sign of fewer active Si particles, which contributed to the capacity decrease leading up to cell failure. The 3D volumetric reconstructions of the electrode at various stages of cycling complemented the observations made from the 2D datasets. The volumetric expansion of the electrode after the initial lithiation was clearly observed in the 3D reconstruction at that state, and the reduced number of reconstructed particles after cycling further indicated that the rapid capacity fade is due to the loss of electrically conducting active Si particles. In future work, this approach can be readily extended to composite graphite−Si electrodes as well as other alloying anodes, such as tin-based anodes.

ASSOCIATED CONTENT

Supporting Information

The Supporting Information is available free of charge at https://pubs.acs.org/doi/10.1021/acsaem.0c02823.

Video SV1 shows the *operando* X-ray radiograph sequence acquired during the initial cycle of the Si electrode as described in Figure 2, playing at 300 frames per second (MP4)

Video SV2 shows the *operando* X-ray radiograph sequence acquired during the higher current density cycling (2^{nd}−15^{th} cycle) of the Si electrode as described in Figure 4, playing at 180 frames per second (MP4)

Video SV3 shows the 3D volumetric reconstructions and their respective orthogonal slices of the Si electrode at six states shown in Figure 7 (MP4)

AUTHOR INFORMATION

Corresponding Author

Shawn Litster − *Department of Mechanical Engineering, Carnegie Mellon University, Pittsburgh, Pennsylvania 15213, United States;* orcid.org/0000-0003-1973-1834; Email: litster@andrew.cmu.edu

Authors

Paul Choi − *Department of Mechanical Engineering, Carnegie Mellon University, Pittsburgh, Pennsylvania 15213, United States*

Bharathy S. Parimalam − *Department of Mechanical Engineering, Carnegie Mellon University, Pittsburgh, Pennsylvania 15213, United States*

Laisuo Su − *Department of Mechanical Engineering, Carnegie Mellon University, Pittsburgh, Pennsylvania 15213, United States*

B. Reeja Jayan − *Department of Mechanical Engineering, Carnegie Mellon University, Pittsburgh, Pennsylvania 15213, United States;* orcid.org/0000-0002-6959-6290

Complete contact information is available at: https://pubs.acs.org/10.1021/acsaem.0c02823

Notes

The authors declare no competing financial interest.

ACKNOWLEDGMENTS

This material is based upon work supported by the National Science Foundation under grant no. 1705321, the National Science Foundation CAREER Award (no. 1751605), and the Wilton E. Scott Institute for Energy Innovation at Carnegie Mellon University. The acquisition of the nano-CT instrument (UltraXRM-L200) was supported by the National Science Foundation MRI grant no. 1229090. Any opinions, findings, and conclusions or recommendations expressed in this material are those of the author(s) and do not necessarily reflect the views of the National Science Foundation.

REFERENCES

(1) Tarascon, J. M.; Armand, M. Issues and Challenges Facing Rechargeable Lithium Batteries. *Nature* **2001**, 359−367.

(2) Obrovac, M. N.; Christensen, L. Structural Changes in Silicon Anodes during Lithium Insertion/Extraction. *Electrochem. Solid-State Lett.* **2004**, *7*, A93−A96.

(3) Hatchard, T. D.; Dahn, J. R. In Situ XRD and Electrochemical Study of the Reaction of Lithium with Amorphous Silicon. *J. Electrochem. Soc.* **2004**, *151*, A838.

(4) Zhang, W. J. A Review of the Electrochemical Performance of Alloy Anodes for Lithium-Ion Batteries. *J. Power Sources* **2011**, *196*, 13−24.

(5) Liang, B.; Liu, Y.; Xu, Y. Silicon-Based Materials as High Capacity Anodes for next Generation Lithium Ion Batteries. *J. Power Sources* **2014**, *267*, 469−490.
(6) Beaulieu, L. Y.; Eberman, K. W.; Turner, R. L.; Krause, L. J.; Dahn, J. R. Colossal Reversible Volume Changes in Lithium Alloys. *Electrochem. Solid-State Lett.* **2001**, *4*, A137.
(7) Obrovac, M. N.; Krause, L. J. Reversible Cycling of Crystalline Silicon Powder. *J. Electrochem. Soc.* **2007**, *154*, A103.
(8) Liu, X. H.; Zhong, L.; Huang, S.; Mao, S. X.; Zhu, T.; Huang, J. Y. Size-Dependent Fracture of Silicon Nanoparticles during Lithiation. *ACS Nano* **2012**, *6*, 1522−1531.
(9) Ryu, J. H.; Kim, J. W.; Sung, Y. E.; Oh, S. M. Failure Modes of Silicon Powder Negative Electrode in Lithium Secondary Batteries. *Electrochem. Solid-State Lett.* **2004**, *7*, A306−A309.
(10) Oumellal, Y.; Delpuech, N.; Mazouzi, D.; Dupré, N.; Gaubicher, J.; Moreau, P.; Soudan, P.; Lestriez, B.; Guyomard, D. The Failure Mechanism of Nano-Sized Si-Based Negative Electrodes for Lithium Ion Batteries. *J. Mater. Chem.* **2011**, *21*, 6201−6208.
(11) McDowell, M. T.; Lee, S. W.; Harris, J. T.; Korgel, B. A.; Wang, C.; Nix, W. D.; Cui, Y. In Situ TEM of Two-Phase Lithiation of Amorphous Silicon Nanospheres. *Nano Lett.* **2013**, *13*, 758−764.
(12) Gu, M.; Li, Y.; Li, X.; Hu, S.; Zhang, X.; Xu, W.; Thevuthasan, S.; Baer, D. R.; Zhang, J. G.; Liu, J.; Wang, C. In Situ TEM Study of Lithiation Behavior of Silicon Nanoparticles Attached to and Embedded in a Carbon Matrix. *ACS Nano* **2012**, *6*, 8439−8447.
(13) Breitung, B.; Baumann, P.; Sommer, H.; Janek, J.; Brezesinski, T. In Situ and Operando Atomic Force Microscopy of High-Capacity Nano-Silicon Based Electrodes for Lithium-Ion Batteries. *Nanoscale* **2016**, *8*, 14048−14056.
(14) Becker, C. R.; Strawhecker, K. E.; McAllister, Q. P.; Lundgren, C. A. In Situ Atomic Force Microscopy of Lithiation and Delithiation of Silicon Nanostructures for Lithium Ion Batteries. *ACS Nano* **2013**, *7*, 9173−9182.
(15) Pietsch, P.; Hess, M.; Ludwig, W.; Eller, J.; Wood, V. Combining Operando Synchrotron X-Ray Tomographic Microscopy and Scanning X-Ray Diffraction to Study Lithium Ion Batteries. *Sci. Rep.* **2016**, *6*, 1−10.
(16) Sun, F.; Markötter, H.; Dong, K.; Manke, I.; Hilger, A.; Kardjilov, N.; Banhart, J. Investigation of Failure Mechanisms in Silicon Based Half Cells during the First Cycle by Micro X-Ray Tomography and Radiography. *J. Power Sources* **2016**, *321*, 174−184.
(17) Taiwo, O. O.; Eastwood, D. S.; Lee, P. D.; Paz-Garcia, J. M.; Hall, S. A.; Brett, D. J. L.; Shearing, P. R. In-Situ Examination of Microstructural Changes within a Lithium-Ion Battery Electrode Using Synchrotron X-Ray Microtomography. *ECS Trans.* **2015**, *69*, 81−85.
(18) Tariq, F.; Yufit, V.; Eastwood, D. S.; Merla, Y.; Biton, M.; Wu, B.; Chen, Z.; Freedman, K.; Offer, G.; Peled, E.; Lee, P. D.; Golodnitsky, D.; Brandon, N. In-Operando X-Ray Tomography Study of Lithiation Induced Delamination of Si Based Anodes for Lithium-Ion Batteries. *ECS Electrochem. Lett.* **2014**, *3*, A76−A78.
(19) Taiwo, O. O.; Paz-García, J. M.; Hall, S. A.; Heenan, T. M. M.; Finegan, D. P.; Mokso, R.; Villanueva-Pérez, P.; Patera, A.; Brett, D. J. L.; Shearing, P. R. Microstructural Degradation of Silicon Electrodes during Lithiation Observed via Operando X-Ray Tomographic Imaging. *J. Power Sources* **2017**, *342*, 904−912.
(20) Taiwo, O. O.; Loveridge, M.; Beattie, S. D.; Finegan, D. P.; Bhagat, R.; Brett, D. J. L.; Shearing, P. R. Investigation of Cycling-Induced Microstructural Degradation in Silicon-Based Electrodes in Lithium-Ion Batteries Using X-Ray Nanotomography. *Electrochim. Acta* **2017**, *253*, 85−92.
(21) Schindelin, J.; Arganda-Carreras, I.; Frise, E.; Kaynig, V.; Longair, M.; Pietzsch, T.; Preibisch, S.; Rueden, C.; Saalfeld, S.; Schmid, B.; Tinevez, J. Y.; White, D. J.; Hartenstein, V.; Eliceiri, K.; Tomancak, P.; Cardona, A. Fiji: An Open-Source Platform for Biological-Image Analysis. *Nat. Methods* **2012**, *9*, 676−682.
(22) Tseng, Q. Template Matching and Slice Alignment -- ImageJ Plugins. **2011**.
(23) Gürsoy, D.; De Carlo, F.; Xiao, X.; Jacobsen, C. TomoPy: A Framework for the Analysis of Synchrotron Tomographic Data. *J. Synchrotron Radiat.* **2014**, *21*, 1188−1193.
(24) Pelt, D. M.; Gürsoy, D.; Palenstijn, W. J.; Sijbers, J.; De Carlo, F.; Batenburg, K. J. Integration of TomoPy and the ASTRA Toolbox for Advanced Processing and Reconstruction of Tomographic Synchrotron Data. *J. Synchrotron Radiat.* **2016**, *23*, 842−849.
(25) Buades, A.; Coll, B.; Morel, J. M. A Non-Local Algorithm for Image Denoising. In *Proceedings - 2005 IEEE Computer Society Conference on Computer Vision and Pattern Recognition, CVPR 2005*; IEE, 2005; pp 60−65, DOI: 10.1109/CVPR.2005.38.
(26) Ollion, J.; Cochennec, J.; Loll, F.; Escudé, C.; Boudier, T. TANGO: A Generic Tool for High-Throughput 3D Image Analysis for Studying Nuclear Organization. *Bioinformatics* **2013**, *29*, 1840−1841.
(27) Jiang, Y.; Hanwell, M. D.; Padgett, E.; Waldon, S.; Muller, D. A.; Hovden, R. Advanced Platform for 3D Visualization, Reconstruction, and Segmentation with Electron Tomography. *Microsc. Microanal.* **2016**, *22*, 2070−2071.
(28) Frisco, S.; Kumar, A.; Whitacre, J. F.; Litster, S. Understanding Li-Ion Battery Anode Degradation and Pore Morphological Changes through Nano-Resolution X-Ray Computed Tomography. *J. Electrochem. Soc.* **2016**, *163*, A2636−A2640.

https://dx.doi.org/10.1021/acsaem.0c02823
ACS Appl. Energy Mater. XXXX, XXX, XXX−XXX